Synergistic Optimization of Surface Reconstruction and Active Site Construction: GaAs/NiO/$Cu(OH)_2$ for Photoelectrochemical Water Splitting

Yanling Wang,[ab] JunKun Wang,[abc] Wentao Qu,[d] Jiehui Liang,[abc] Shaohua Xie,[ab] Xiangrong Li,[ab] Dongman Hou,[c] Wenliang Wang,*[ab] Guoqiang Li,*[abc]*

a State Key Laboratory of Luminescent Materials and Devices, South China University of Technology, Guangzhou 510640, China.

b Department of Electronic Materials, School of Materials Science and Engineering, South China University of Technology, Guangzhou 510640, China.

c School of Physics and Optoelectronics, South China University of Technology, Guangzhou 510640, China.

d *Saint Anthony's High School, Saint Anthony 83445, United States of America.*

* Corresponding author, E-mail: houdm@scut.edu.cn, wenliangwang@scut.edu.cn and msgli@scut.edu.cn

Materials characterization

The morphology of the photoelectrodes have been characterized using field emission scanning electron microscopy (FE-SEM, Hitachi SU-8020) and high-resolution transmission electron microscopy (HRTEM, FEI talos F200X). The element binding energy of these photoelectrodes was analysed by X-ray photoelectron spectroscopy (XPS, JEOL, JPS-9200). X-ray diffraction (XRD, Rigaku, Miniflex 600) spectroscopy was carried out to detect the crystal structures of these samples. Raman spectroscopy (Raman, Renishaw inVia) with excitation of 532 nm was utilised for the purpose of detecting the structures of GaAs/Ni-NiO. A UV-Vis-NIR spectrophotometer (PerkinElmer, Lambda 950) was employed to investigate the optical properties of these samples. The photogenerated charge carrier dynamics and lifetime of these samples were estimated using fluorescence photoluminescence (PL) and time-resolution PL (TRPL, FLS 980).

PEC measurements

The photoelectrochemical properties of each sample were evaluated using a three-electrode electrochemical workstation (CHI 760E, CH Instruments Inc.) under illumination from a 300 W xenon lamp (100 mW/cm^2) with 0.1 M Na_2SO_4 (pH = 6.10) as the electrolyte. The prepared photoelectrodes were used as working electrodes, Pt electrode as counter electrodes and Ag/AgCl (saturated KCl) electrode as reference electrodes. The effective areas of the photoelectrodes were all about 0.2 cm^2. For comparison purposes, the electrode potentials relative to the Ag/AgCl reference electrode were converted to reversible hydrogen electrode (RHE) potentials in all tests using the conversion relationship[1]

$$E_{RHE} = E_{Ag/AgCl}(ref) + 59\ mV \times pH \#(1)$$

$$E_{Ag/AgCl}(ref) = 0.192\ V \#(2)$$

LSV curves were obtained at a scan rate of 10 mV/s[1] under dark or light

conditions. Electrochemical impedance spectroscopy (EIS) was performed between 1 and 100 kHz at 0 V vs. RHE to study photoelectrode interface reactions and kinetic processes. And the applied bias photon current efficiency (ABPE) of the electrode can be calculated from the LSV curve using the following relationship[2]

$$ABPE = J_{ph}[mA\ cm^{-2}] \times (1.23 - V_{app})[V] \times 100\% / P_{light}[mW\ cm^{-2}] \#(3)$$

where $J_{ph}$is the photocurrent density at the bias voltage, 1.23 is the redox potential of water, $V_{app}$is the bias voltage applied between the working electrode and the Pt electrode, and P_{light} is the incident light intensity.

These samples were subjected to Mott–Schottky (M–S) testing under dark conditions with an amplitude of 35 mV and a frequency of 5 kHz. Based on the curves, the conductivity types of different samples were determined. And the flat band potential (E_{fb}) was obtained using the following relationship[3]

$$1/C_S^2 = 2(E - E_{fb} - kT/e)/\varepsilon\varepsilon_0 Ne \#\ （4）$$

Where C_s refer to the capacitance of the space charge region, ε and ε_0 represent the relative permittivity and vacuum permittivity of semiconductors. N stands for carrier concentration. E and E_{fb} represent applied and flat charged potentials. kT/e is the temperature-dependent term and can be neglected at room temperature.

Carrier lifetime is an important parameter for evaluating the PEC hydrogen production capability of semiconductor materials. The average carrier lifetime in this paper is obtained by fitting a nonlinear quadratic function of Transient Photoluminescence Spectroscopy (TRPL)[4]

$$y = y_0 + A_1 e^{-x/\tau_1} + A_2 e^{--x/\tau_2} \#(5)$$

$$\tau_{ave} = (A_1 t_1^2 + A_2 t_2^2)/(A_1 t_1 + A_2 t_2) \#(6)$$

Where A_1 and A_2 are the prefactors, t_1 and t_2 are the relaxation times, τ_{ave} is the average carrier lifetime.

Carrier injection efficiency refers to the efficiency with which photo-generated carriers cross interfaces in optoelectronic devices and participate in target reactions[5]

$$\eta_{injection} = {}^{\eta_{H_2O}}\!/_{\eta_{Na_2SO_3}} \#(7)$$

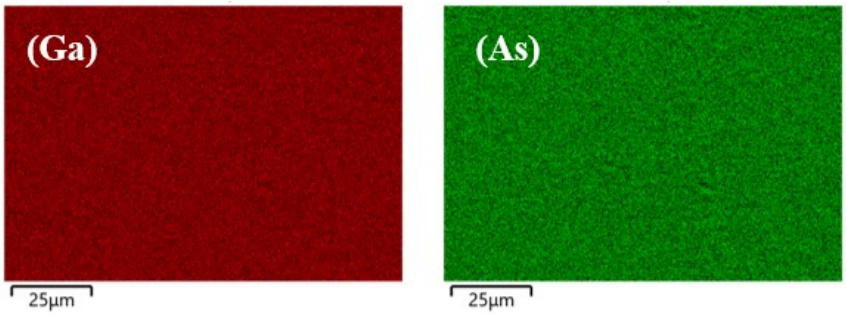

Fig. S1 Ga and As elemental mapping images of GaAs/Ni-NiO.

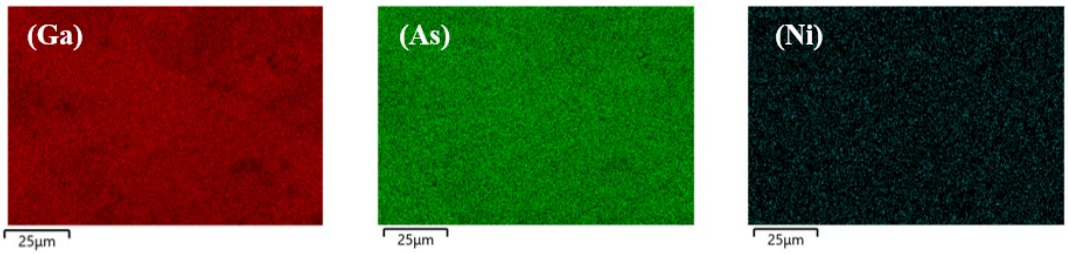

Fig. S2 Ga, As and Ni elemental mapping images of GaAs/NiO/$Cu(OH)_2$.

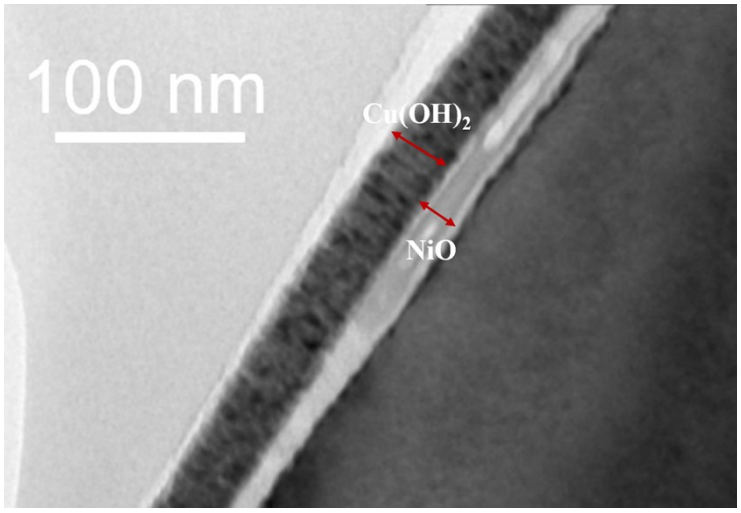

Fig. S3 Cross-sectional HR-TEM images of GaAs/NiO/$Cu(OH)_2$.

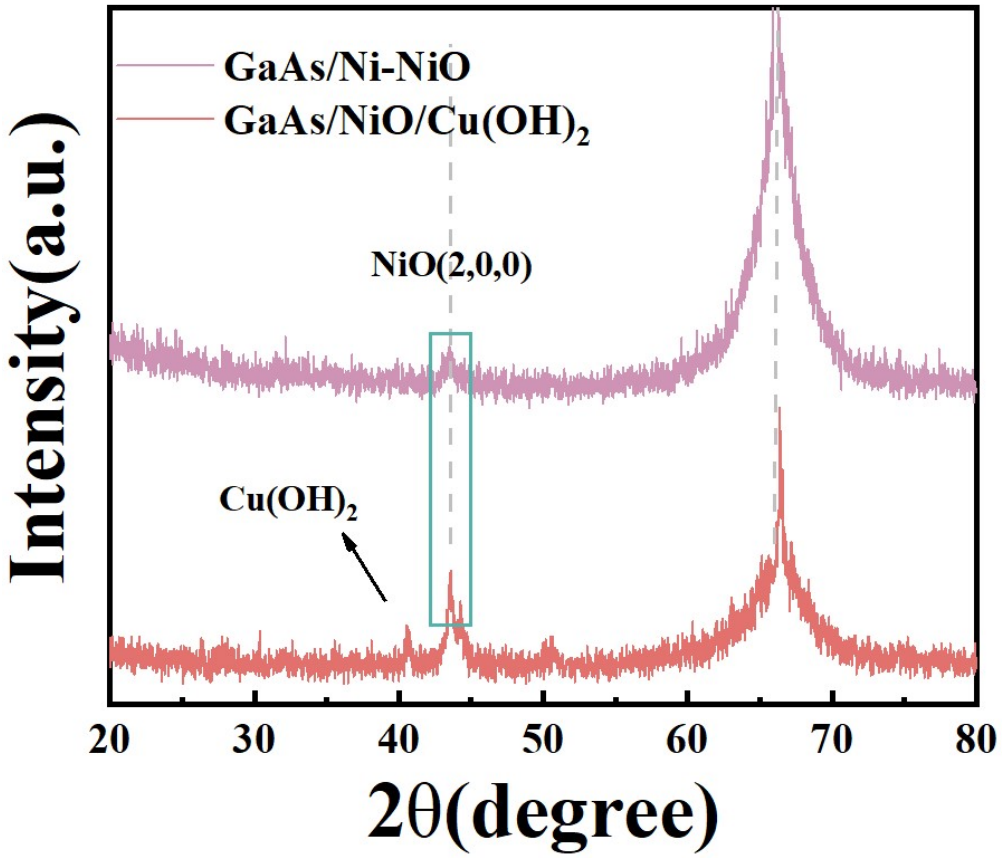

Fig. S4 XRD patterns of GaAs/Ni-NiO and GaAs/NiO/$Cu(OH)_2$.

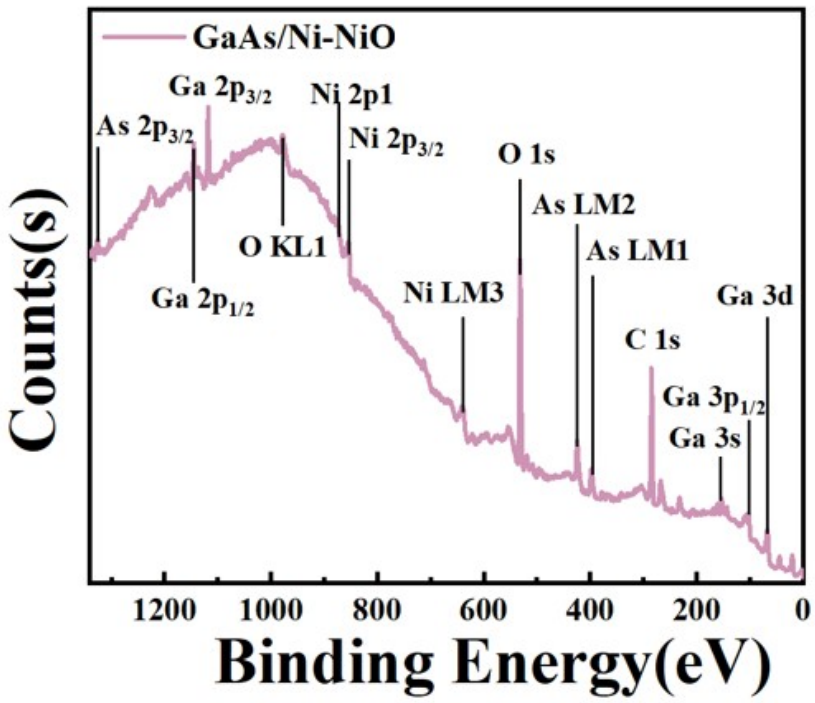

Fig. S5 The survey spectra of GaAs/Ni-NiO.

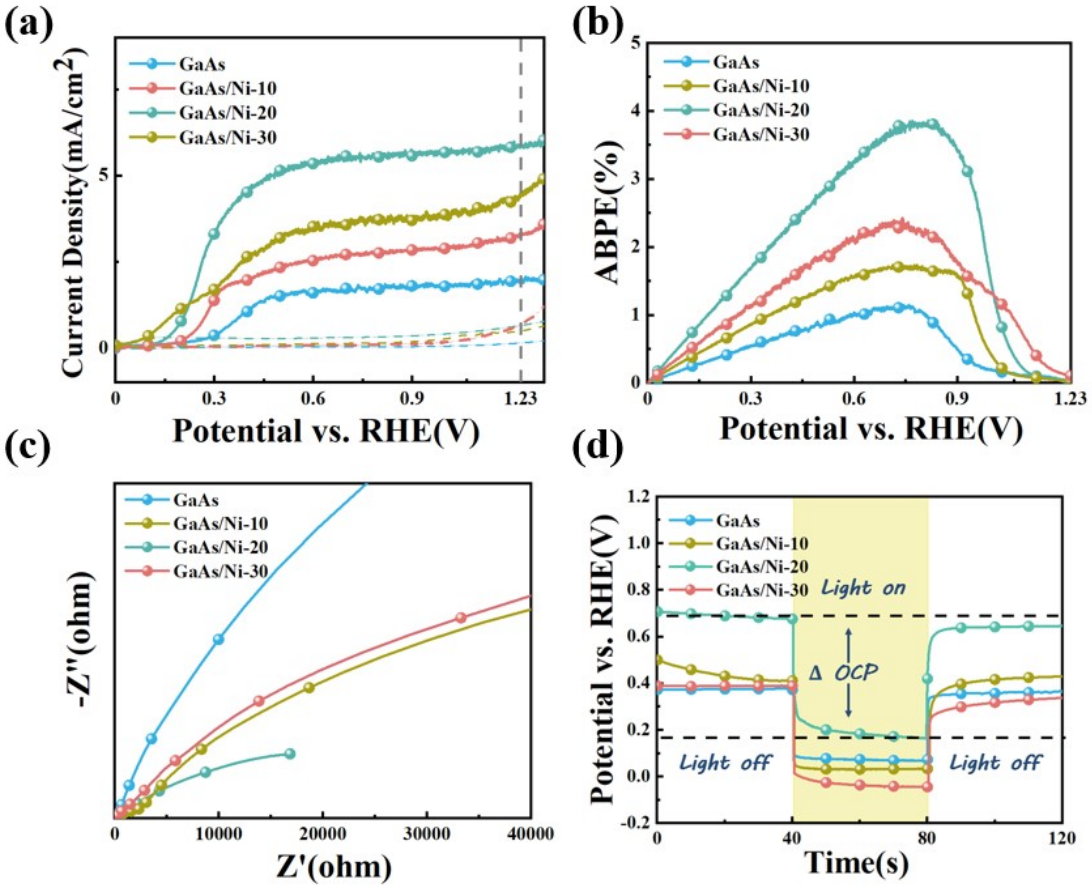

Fig. S6 (a) LSV; (b) ABPE; (c) Nyquist and (d) OCPT of GaAs and GaAs/Ni-x (x=10、20、30). The experiment was replicated on three occasions in order to obtain the results.

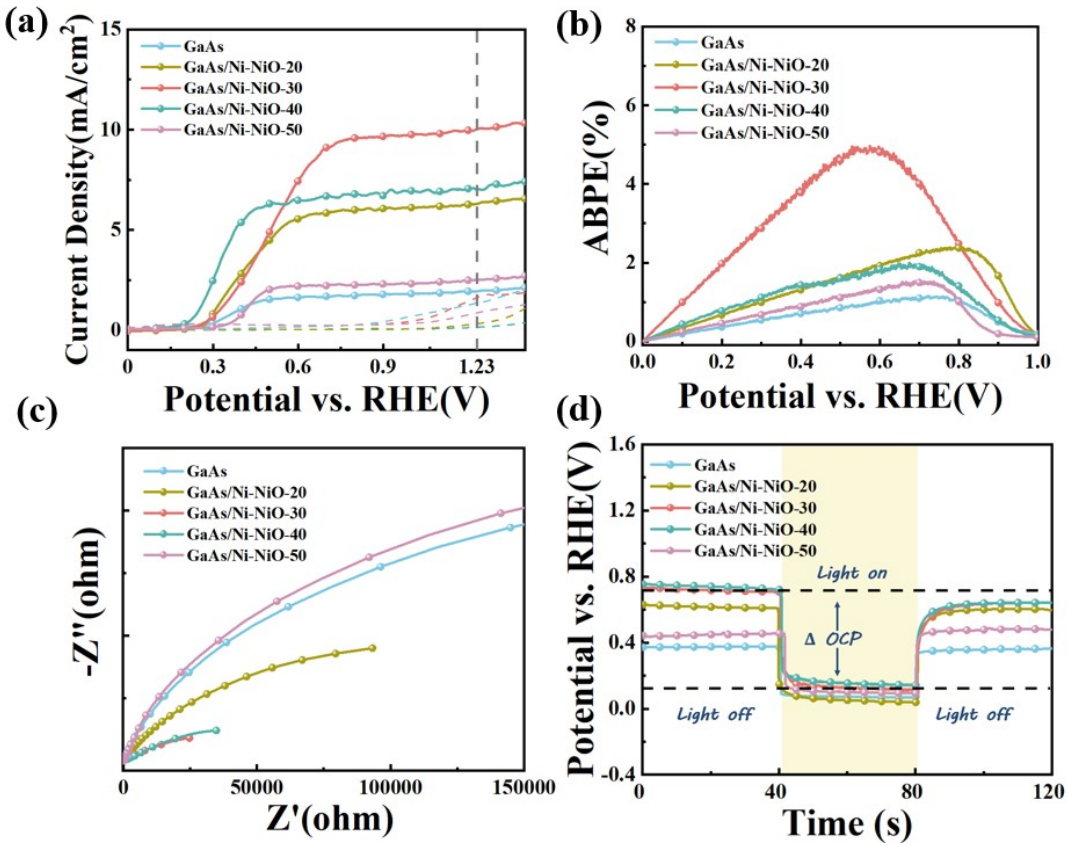

Fig. S7 (a) LSV; (b) ABPE; (c) Nyquist and (d) OCPT of GaAs and GaAs/NiO-x (x=20、30、40、50). Modification range: 0.35–0.75 V vs. Ag/AgCl.

The experiment was replicated on three occasions in order to obtain the results.

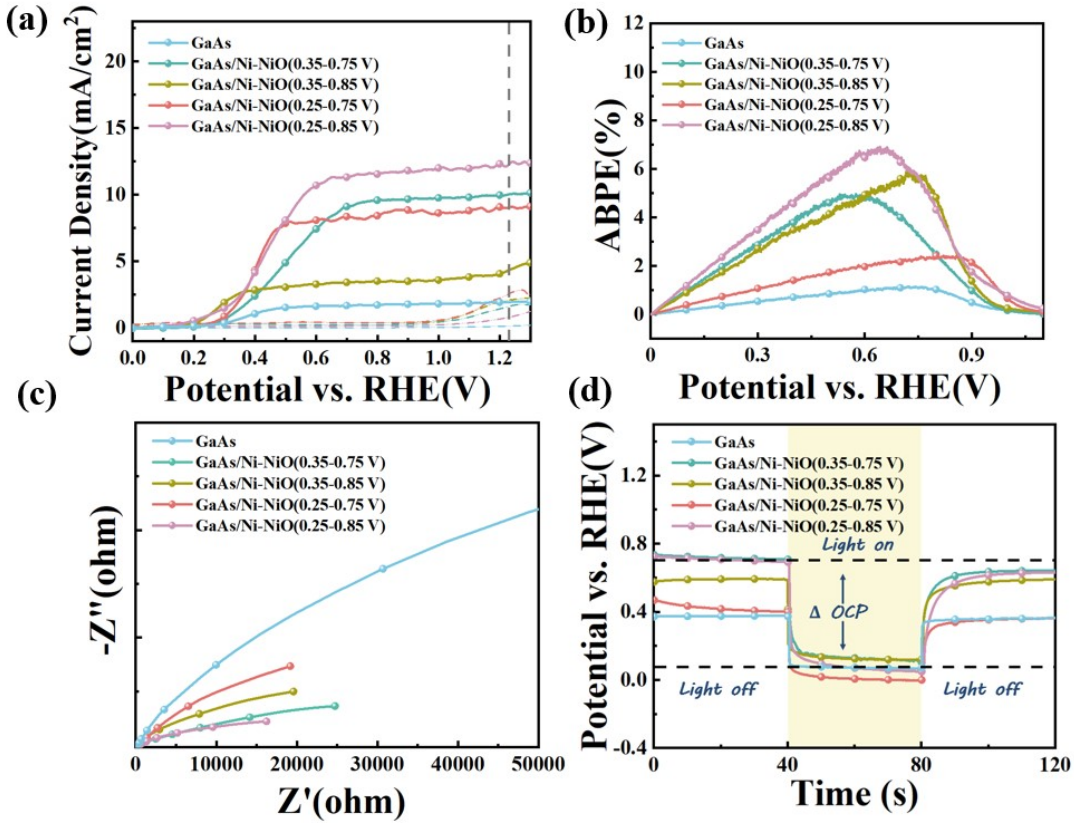

Fig. S8 (a)LSV; (b)ABPE; (c)Nyquist and (d)OCPT of GaAs and GaAs/NiO (x-y V) (x=0.25、0.35, y=0.75、0.85). Modified wheel count: 30.

The experiment was replicated on three occasions in order to obtain the results.

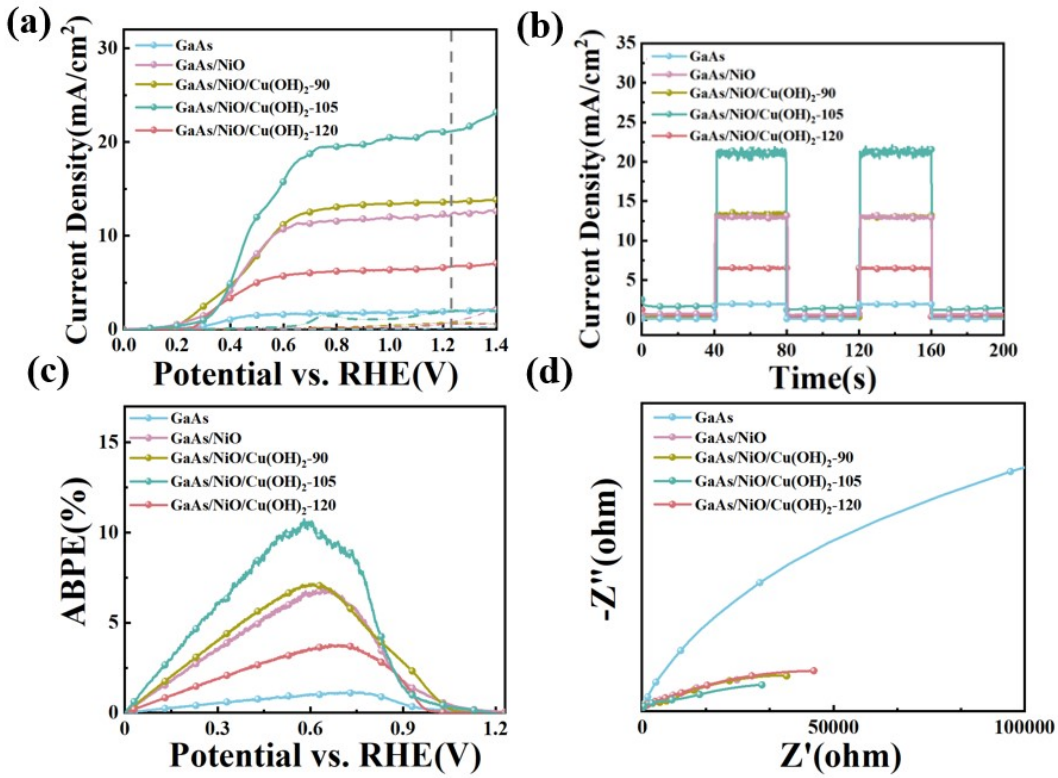

Fig. S9 (a) LSV; (b)I-t; (c) ABPE and (d) Nyquist of GaAs、GaAs/NiO and GaAs/NiO/Cu(OH)$_2$-x(x=90、105、120). Deposition current is 5 mA/cm^2.

The experiment was replicated on three occasions in order to obtain the results.

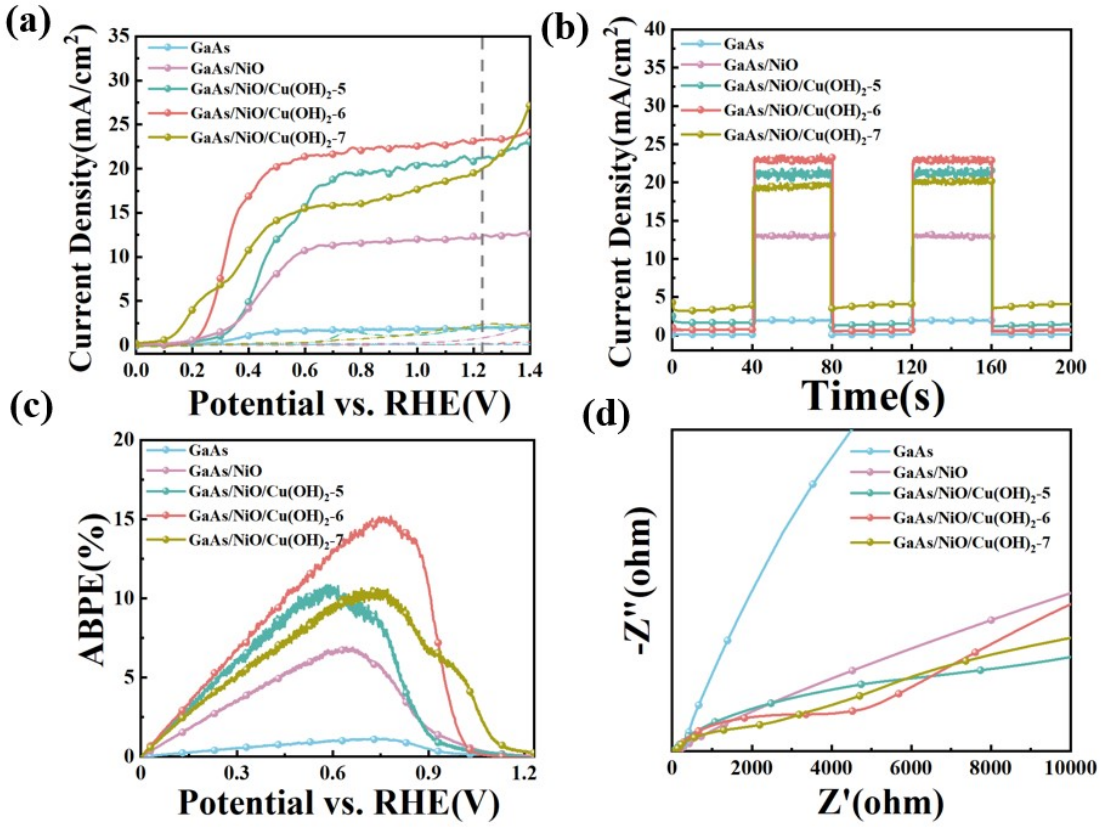

Fig. S10 (a)LSV; (b)I-t; (c)ABPE and (d) Nyquist of GaAs、GaAs/NiO and GaAs/NiO/Cu(OH)$_2$ x(x=5,6,7). Deposition time: 105s.

The experiment was replicated on three occasions in order to obtain the results.

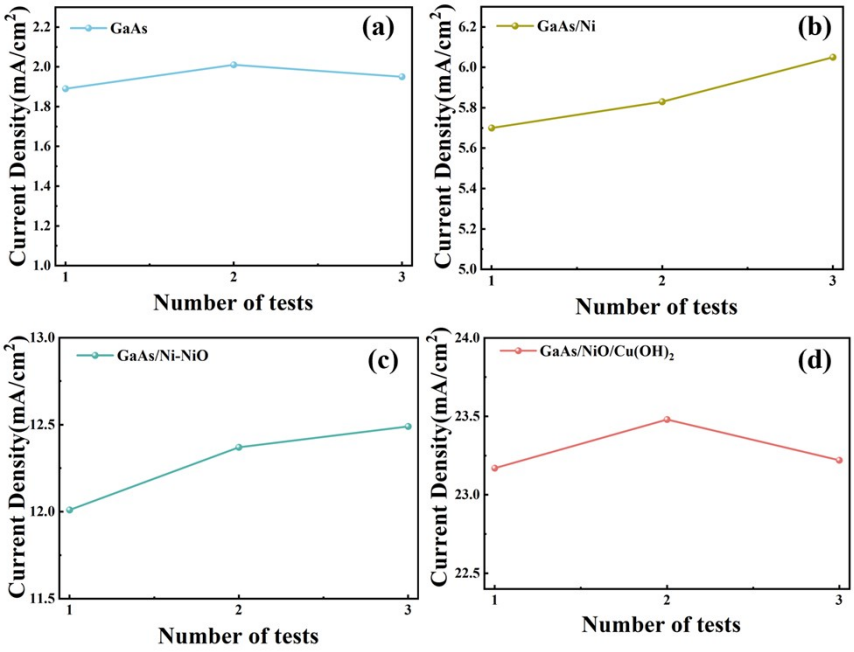

Fig. S11 Under a bias voltage of 1.23 V vs. RHE, three repeatability tests were conducted on different electrodes, yielding the following current density results: (a) GaAs electrode, (b) GaAs/Ni electrode, (c) GaAs/Ni-NiO electrode and (d) GaAs/NiO/Cu(OH)$_2$ electrode.

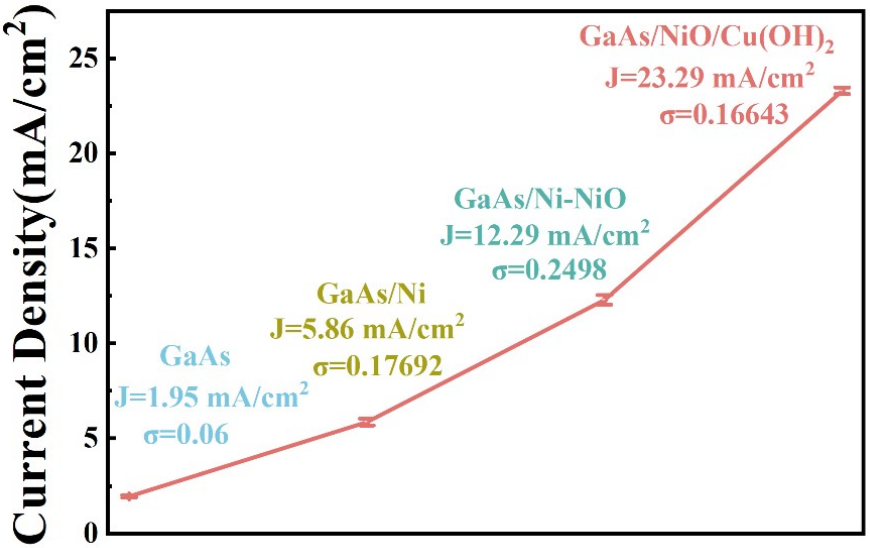

Fig. S12 Average and standard deviation of photocurrent density at 1.23 V vs. RHE bias for different electrodes.

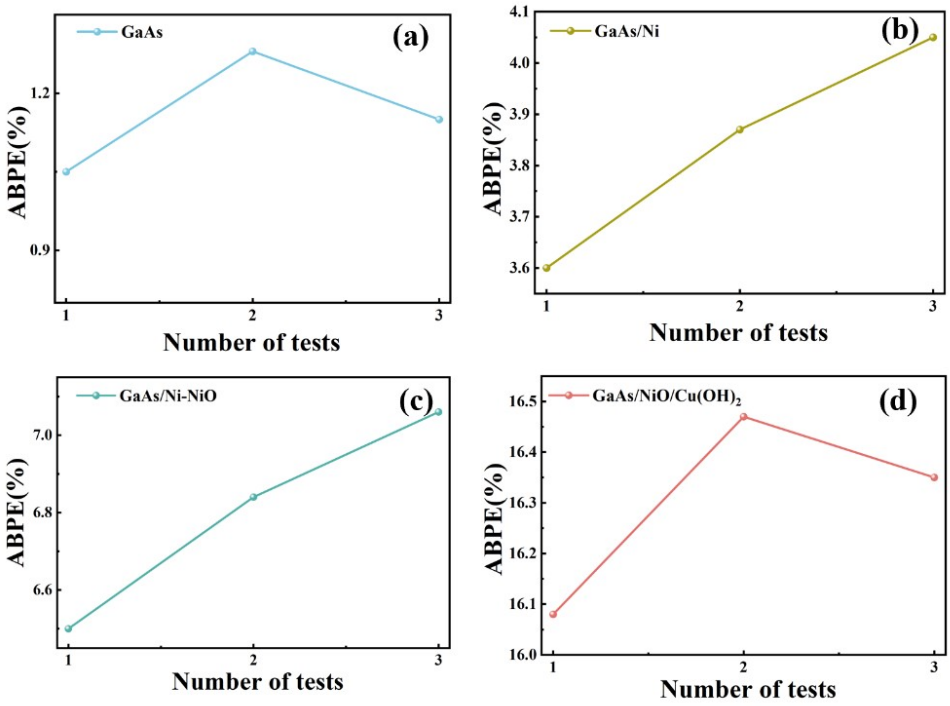

Fig. S13 ABPE values obtained from three repeated tests with different electrodes: (a) GaAs electrode, (b) GaAs/Ni electrode, (c) GaAs/Ni-NiO electrode and (d) GaAs/NiO/$Cu(OH)_2$ electrode.

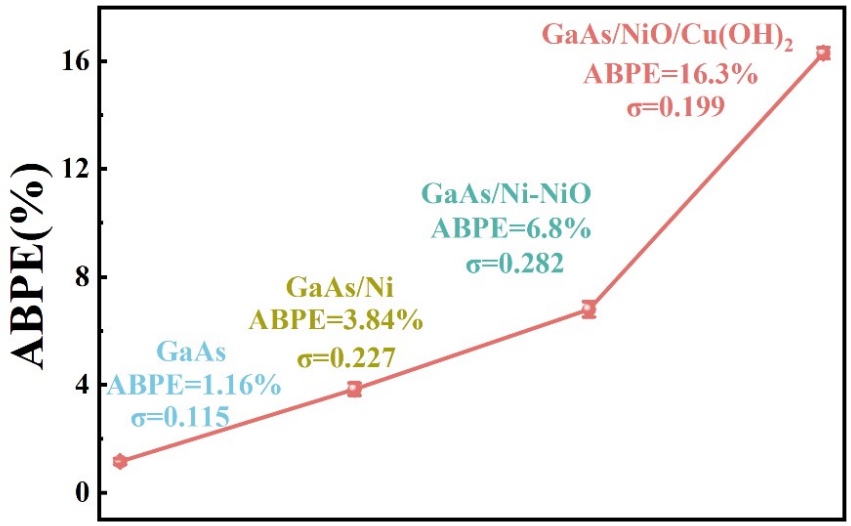

Fig. S14 Average and standard deviation of ABPE for different electrodes.

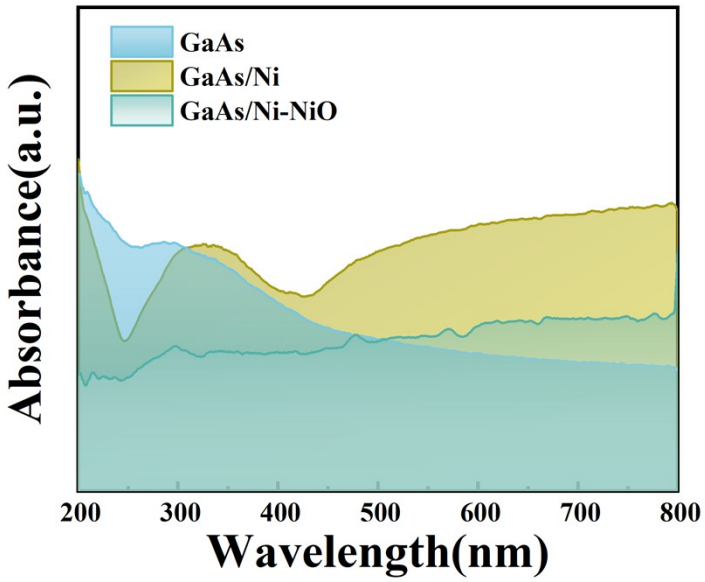

Fig. S15 UV–Vis DRS spectra of GaAs、GaAs/Ni and GaAs/Ni-NiO.

To elucidate the SPR effect of Ni, we analyzed the UV-visible diffuse reflectance spectra of the GaAs/Ni electrode in the 200–800 nm range, with the results shown in Fig. S15. Compared to pure GaAs and GaAs/Ni-NiO photoelectrodes, the GaAs/Ni electrode exhibits significantly enhanced broadband absorption capability in the 300–800 nm visible light spectrum. This phenomenon indicates that the presence of the Ni metal layer extends the electrode's response range to low-energy, long-wavelength visible light in the 400–800 nm region of the solar spectrum, thereby further corroborating the SPR effect of Ni metal. Within the 200–300 nm ultraviolet wavelength range, high-energy photons exhibit a pronounced interaction with free electrons in the Ni film, resulting in a specific attenuation in light absorption intensity within this region. This interaction forms a distinct absorption valley near 250 nm. Furthermore, the absorbance of the GaAs/Ni electrode is significantly higher than that of the GaAs/Ni-NiO electrode, indicating that the presence of the NiO layer suppresses the SPR effect of the Ni metal. When Ni is partially oxidized to NiO, its free electron concentration decreases, weakening the localized electromagnetic field excited by SPR and consequently reducing its light absorption capacity.

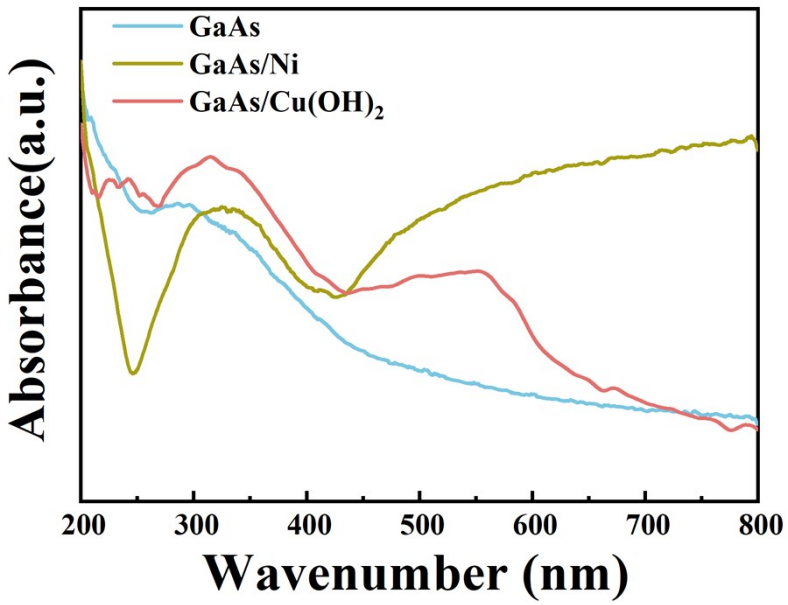

Fig. S16 UV–Vis DRS spectra of GaAs、GaAs/Ni and GaAs/$Cu(OH)_2$.

Fig. S16 shows the UV–Vis DRS spectra of GaAs, GaAs/Ni and GaAs/$Cu(OH)_2$ across the 200–800 nm wavelength range. In contrast to GaAs/Ni, GaAs/$Cu(OH)_2$ shows no absorption dip at 250 nm. This further confirms that this dip originates from the interaction between free electrons in Ni and incident photons. Within the visible light spectrum (400–800 nm), both GaAs and GaAs/$Cu(OH)_2$ demonstrate a gradual reduction in light absorption intensity as the wavelength increases. In contrast, the light absorption intensity of GaAs/Ni increases significantly with wavelength. This difference in absorption behaviour confirms the presence of the SPR effect in Ni. Additionally, the absorption spectrum of the GaAs/$Cu(OH)_2$ photoelectrode exhibits a characteristic minor peak at 550 nm, which is attributed to the d-d electron transition of Cu^{2+} in $Cu(OH)_2$.[6]

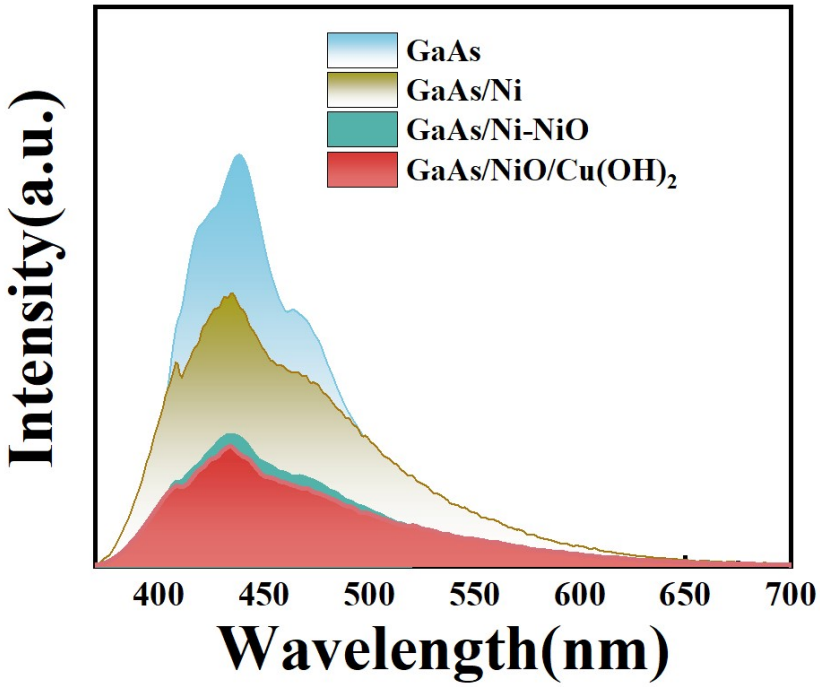

Fig. S17 The PL spectra of all electrodes.

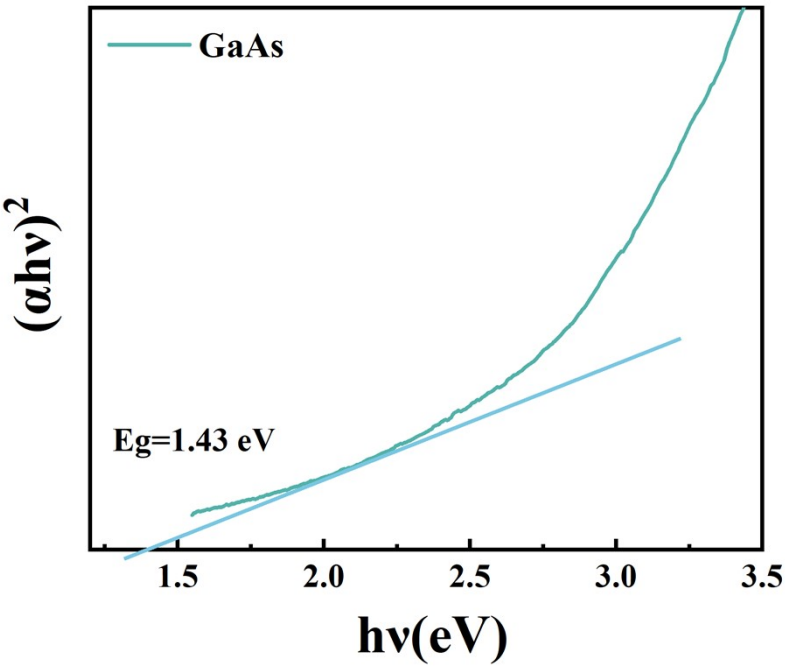

Fig. S18 Tauc plots of GaAs.

Table S1. Summary of the PEC performance of heterojunction photoelectrodes under illumination of 100 mW cm^{-2} with AM 1.5G filter.

photoelectrodes	Electrolyte	H_2 evolution (umol h^{-1})	Refs.
GaAs/NiO/$Cu(OH)_2$	0.1 M Na_2SO_4	198.2	This work
GaAs/Ni-NiO	0.1 M Na_2SO_4	122.4	This work
InGaP/GaAs	0.5 M KOH	128.5	[7]
InN/Ag/UiO-66-$(OH)_2$	0.1 M Na_2SO_4	109.2	[8]
InN/UiO-66-$(OH)_2$	0.1 M Na_2SO_4	39.6	[8]
InN/PM6/NiFe LDH	0.1 M KOH	68.88	[9]
Et-GaAs/TiO_2/Ni-Pi	1.0 M NaOH	103.75	[10]
$In_{0.46}Ga_{0.54}N$/Si	0.5 M H_2SO_4	3.4	[11]
Ni-doped InN/GaZnON	0.5 M Na_2SO_4	2.23	[12]
ZnO:InN	0.5 M Na_2SO_4	0.8	[13]

references

1 J. Lin, Y. Yu, Z. Zhang, F. Gao, S. Liu, W. Wang and G. Li, *Adv Funct Materials*, 2020, **30**, 1910479.

2 Y. Ma, Y. Liu, Y. Bian, A. Zhu, Y. Yang and J. Pan, *Journal of Colloid and Interface Science*, 2018, **518**, 140–148.

3 Q. Rui, L. Wang, Y. Zhang, C. Feng, B. Zhang, S. Fu, H. Guo, H. Hu and Y. Bi, *J. Mater. Chem. A*, 2018, **6**, 7021–7026.

4 B. Yang, C. Ru, Y. Jiao, L. Gao, Y. Song, Z. Hu and J. Hou, *J. Mater. Chem. A*, 2024, **12**, 28521–28530.

5 H. Lee, G.-S. Kang, H. Lim, H. Han, T. W. Kim, J.-H. Choi, D.-G. Choi, J.-Y. Jung, J.-H. Jeong, J. H. Park and J. Lee, *J. Mater. Chem. A*, 2024, **12**, 27246–27256.

6 P. Madhusudan, Y. Wang, B. N. Chandrashekar, W. Wang, J. Wang, J. Miao, R. Shi, Y. Liang, G. Mi and C. Cheng, *Applied Catalysis B: Environmental*, 2019, **253**, 379–390.

7 P. Varadhan, H.-C. Fu, Y.-C. Kao, R.-H. Horng and J.-H. He, *Nat Commun*, 2019, **10**, 5282.

8 X. Li, S. Xie, D. Hou, W. Wang and G. Li, *Journal of Colloid and Interface Science*, 2025, **685**, 573–583.

9 S. Xie, J. Liang, Q. Liu, P. Liu, J. Wang, J. Li, H. Wu, W. Wang and G. Li, *J. Mater. Chem. A*, 2023, **11**, 25671–25682.

10 M. Arunachalam, R. S. Kanase, K. Zhu and S. H. Kang, *Nat Commun*, 2023, **14**, 5429.

11 S. Vanka, B. Zhou, R. A. Awni, Z. Song, F. A. Chowdhury, X. Liu, H. Hajibabaei, W. Shi, Y. Xiao, I. A. Navid, A. Pandey, R. Chen, G. A. Botton, T. W. Hamann, D. Wang, Y. Yan and Z. Mi, *ACS Energy Lett.*, 2020, **5**, 3741–3751.

12 X. Hou, S. Jiang, Y. Li, J. Xiao and Y. Li, *International Journal of Hydrogen Energy*, 2015, **40**, 15448–15453.

13 S. S. Menon, H. Y. Hafeez, B. Gupta, K. Baskar, G. Bhalerao, S. Hussain, B. Neppolian and S. Singh, *Renewable Energy*, 2019, **141**, 760–769.